Refractive Index Tuning of All-Inorganic TiO₂
Nanocrystal-Based Films and High Aspect Ratio
Nanostructures Using Atomic Layer Deposition:
Implications for High-Throughput Fabrication of
Metalenses

Dae Eon Jung¹, Irene R. Howell¹, Vincent J. Einck¹, Feyza Dundar Arisoy¹, Lucas D. Verrastro¹, Andrew McClung², Amir Arbabi², and James J. Watkins^{1,*}

¹Department of Polymer Science and Engineering, University of Massachusetts, Amherst,
Massachusetts 01003, United States

²Department of Electrical and Computer Engineering, University of Massachusetts, Amherst, Massachusetts 01003, United States

Submitted to ACS Applied Nano Materials

*Email: watkins@polysci.umass.edu

Abstract

High refractive index (RI) components and nanostructures are of great interest for compact optics, waveguides, photonics and metamaterials. Herein we demonstrate that atomic layer deposition (ALD) can be used as a short, post-fabrication step to dramatically increase the RI of nanocrystal (NC)-based films and patterned nanostructures in conjunction with a single-step, direct nanoimprint lithography (NIL). The initial RI of TiO_2 NC-based films was n = 1.95 at 543 nm which can then be increased to 2.00 by post calcination and further up to 2.15 by TiO₂ ALD. 15 cycles of ALD were sufficient to achieve this rapid increase of RI and any intermediate RI value can be tuned by adjusting the number of ALD cycles accordingly. Nanoscale interstitial gaps between TiO₂ NCs allowed a uniform diffusion of ALD precursors, resulting in a much denser structure and the RI increase. An array of 4 mm-sized metalenses was fabricated to demonstrate the effects of the RI tuning on the performance of optical devices. The focusing efficiencies of the as-imprinted metalenses (smallest dimension ~ 80 nm, highest aspect ratio ~ 8) were 61% on average but the post-treatments including calcination and ALD significantly increased the average efficiency to 67%, and up to 75% for the best-performing lens. This approach combines the fast, scalable, and versatile, solvent-assisted NIL method to pattern optical nanostructures with a short, post-patterning deposition and densification step that significantly enhances optical performance.

Keywords

Metalenses, Metasurface, Atomic layer deposition, Nanoimprint lithography, Refractive index tuning, Additive manufacturing, High-throughput manufacturing, Nanocrystal composites

Introduction

The design and fabrication of nanopatterned surfaces for compact and planar optics is an area of growing interest and importance. For example, metalenses are ultrathin planar (flat) lenses comprising dissimilar high aspect ratio (HAR) and high refractive index (RI) nanofeatures arranged on a periodic lattice that efficiently diffract light. These lenses can be designed to achieve a desired amplitude, phase, or polarization distribution by tuning size, shape, pitch and material properties and thus offer capabilities that extend beyond traditional lenses in a considerably more compact form factor. Since the efficiency of these metasurfaces relies on the magnitude of RI contrast between two materials (typically the lens materials and air), there is a strong desire to maximize the RI of the optical material to enhance performance and simplify design. A similar challenge presents itself in optical waveguide gratings for augmented reality wherein field of view is directly tied to the RI of the waveguide material and coupling gratings. For visible-light applications, which require transparency throughout the visible spectrum, TiO₂ has been identified as a promising material.

While TiO₂ is a promising candidate for visible-light metasurfaces and compact optics, widespread adoption has been limited due to challenges associated with scalable fabrication and manufacturing pathways. Although TiO₂ is considered to have a high RI, its index is lower than that of materials used analogously in the infrared region, for example the RI of amorphous silicon is 3.95 at 800 nm. Thus, TiO₂-based metasurfaces require more extreme geometrical designs, such as HARs. Recently, Khorasaninejad *et al.*³ reported the fabrication of HAR TiO₂ metalenses using a sequential process including electron beam (e-beam) lithography, atomic layer deposition (ALD) of amorphous TiO₂, reactive ion etching (RIE) to remove excess TiO₂, and the removal of the resist template. ALD is capable of very precise controls over film thickness and deposited composition⁹-

¹⁰ as well as conformal deposition onto HAR structures¹¹. This low-roughness, conformal coating capability due to the self-limiting and sequential character of the ALD process has made ALD a powerful and attractive tool in the fabrication of many nanostructured materials.¹² In the semiconductor industry, highly conformal deposition of a variety of high dielectric constant oxides has helped enable the continued decrease in transistor node size.¹³ In optoelectronics and photovoltaics, the control afforded by ALD in tuning a film's composition with three or more different elements results in control over bandgap, density, conductivity, and more. 14 For fuel cell applications, depositing electrolytes layers by ALD enables reduction in thickness, which in turn enables lower fuel cell operating temperatures through kinetics. 15-16 Despite the conformality of the ALD process, its major drawback when it is used for full feature fabrication is extended processing times. Metalens elements require hundreds or thousands of deposition cycles depending on the feature dimensions being targeted, which limit scalability and throughput. More recently, we reported a fast, scalable route to fabricate TiO₂ nanocrystal (NC)-based metalenses via additive manufacturing, ¹⁷ specifically using a direct, single-step, solvent-assisted nanoimprint lithography (NIL) process, ¹⁸⁻²⁵ as an alternative to the all ALD-based subtractive manufacturing. A processing time of 2 minutes per wafer was achieved and the focusing efficiencies of the metalenses were over 50% for a 400-µm-diameter metalens and 43% for a 4-mm-diameter metalens, demonstrating a novel pathway to fabricate high-throughput metalenses at a rate of 30 wafers per hour.

Here we combined the NIL and ALD processes to fabricate high performance metalenses. NIL provided a direct, single-step route to high-throughput fabrication of metalenses while ALD was then utilized as a post-fabrication step to maximize the optical performance of the NIL-based lenses by boosting the RI of the structures in a rapid and scalable manner. Unlike the time-

consuming ALD process in the subtractive manufacturing, only a few cycles of ALD were employed to accomplish this RI boost and the resultant enhancement of the optical performance.

Results and Discussion

RI tunability of TiO₂ NC-based films

Scheme 1a illustrates the overall fabrication process of all-inorganic TiO₂ films using a TiO₂ NC-dispersed ink and post-treatments including calcination and ALD. The spin coating of the ink onto a substrate followed by pulse UV curing of the spin coated film results in a thin TiO₂ NC-based film composed mostly of inorganic contents. Due to the strong photocatalytic activity of the anatase phase TiO₂ NCs, their UV-activated radicals remove almost all organic moieties in the ligands, residual solvents, and binder through oxidative degradation. Any organic residues are further eliminated completely by calcination at 500°C in air to fabricate environmentally and mechanically stable all-inorganic structures. A dramatic RI increase from this calcined film is then achieved by ALD either onto a planar film or an imprint using the same TiO₂ ALD precursor. As illustrated in Scheme 1b, the calcination of the TiO₂ NC-based film or imprint leaves some voids between densely packed NCs (average diameter of NCs: 8 nm), which provides a few nanometer-sized path for the diffusion of ALD precursors. A small number of ALD cycles was found to be sufficient to backfill these interstitial gaps between TiO₂ NCs by replacing low-index air vacancies with high-index ALD-deposited TiO₂, providing a fast and cost-effective route to RI tuning.

Scheme 1. (a) Schematic illustration of the overall process flows for fabricating all-inorganic TiO₂ nanocrystal-based planar films and imprints *via* post-treatments including calcination and atomic layer deposition (ALD) and (b) more detailed illustration of the backfill process of interstitial gaps between nanocrystals in films and imprints by ALD of TiO₂.

(a) Process flows for fabrication of TiO₂ NC-based planar films and imprints using an elastomeric stamp

SiO, binder

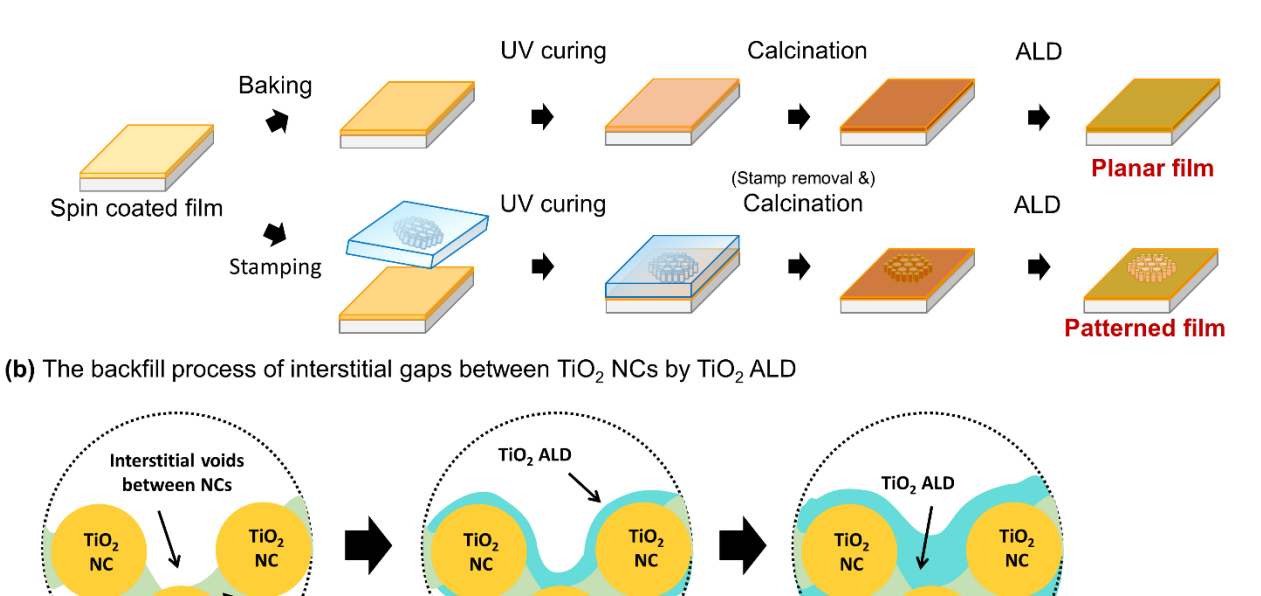


Figure 1a shows the RI and thickness variations of the calcined TiO₂ films with ALD cycles of TiO₂ deposited at 250°C, which were measured by a variable angle spectroscopic ellipsometer (VASE). An abrupt increase of RI is observed in the early stage of the ALD process but the rate of the RI change becomes much slower once it reaches 10 cycles. The film thickness, however, remains almost unchanged below 25 cycles considering some fluctuations of thickness between samples and within each sample. This sharp RI increase without a thickness change indicates that 10 cycles of ALD primarily serve to backfill the interstitial voids between TiO₂ NCs as suggested in Scheme 1b, bringing about the increase of RI from 2.00 (calcined) to 2.15 (10 cycles) at the wavelength of 543 nm which is the target wavelength of the metalens design, as discussed later. Above 25 cycles, the film thickness starts increasing whereas RI increases relatively slowly, implying that the ALD deposition now takes place primarily on the film surface since all accessible

interstitial voids throughout the film have been filled by initial ALD cycles. As illustrated in Figure 1b, the ALD process onto the TiO₂ NC-based film can be largely divided into two stages: (1) the backfill stage of the interstitial gaps between NCs (0-25 cycles) and (2) the cladding stage on the backfilled film surface (≥ 25 cycles). Figure 1c supports this two-stage ALD process. Mean squared error (MSE) values in ellipsometry quantify the difference between experimental and model-generated data. The fitting is considered good for MSE < 10 and still reasonable and acceptable for MSE < 20. In Figure 1c, we compared two different models for the Cauchy transparent film on a Si substrate: the ideal model, which assumes a single homogeneous layer, and a graded model which considers a gradient in RI throughout the thickness of the film. This RI gradient-added model was used to plot Figure 1a. Up to 25 cycles, the films all give MSE values lower than 10 for both models and MSE values are almost the same even after adding the RI gradient function to the ideal model. Little to no improvement in MSE implies there is a negligible degree of RI gradients in films below 25 cycles. Above 50 cycles, the increasing gap between two MSE curves indicates the formation of a cladded layer, that is the second stage in Figure 1b, which prevents good fitting to the ideal Cauchy model, only suitable for transparent and homogeneous films without any gradient in RI.

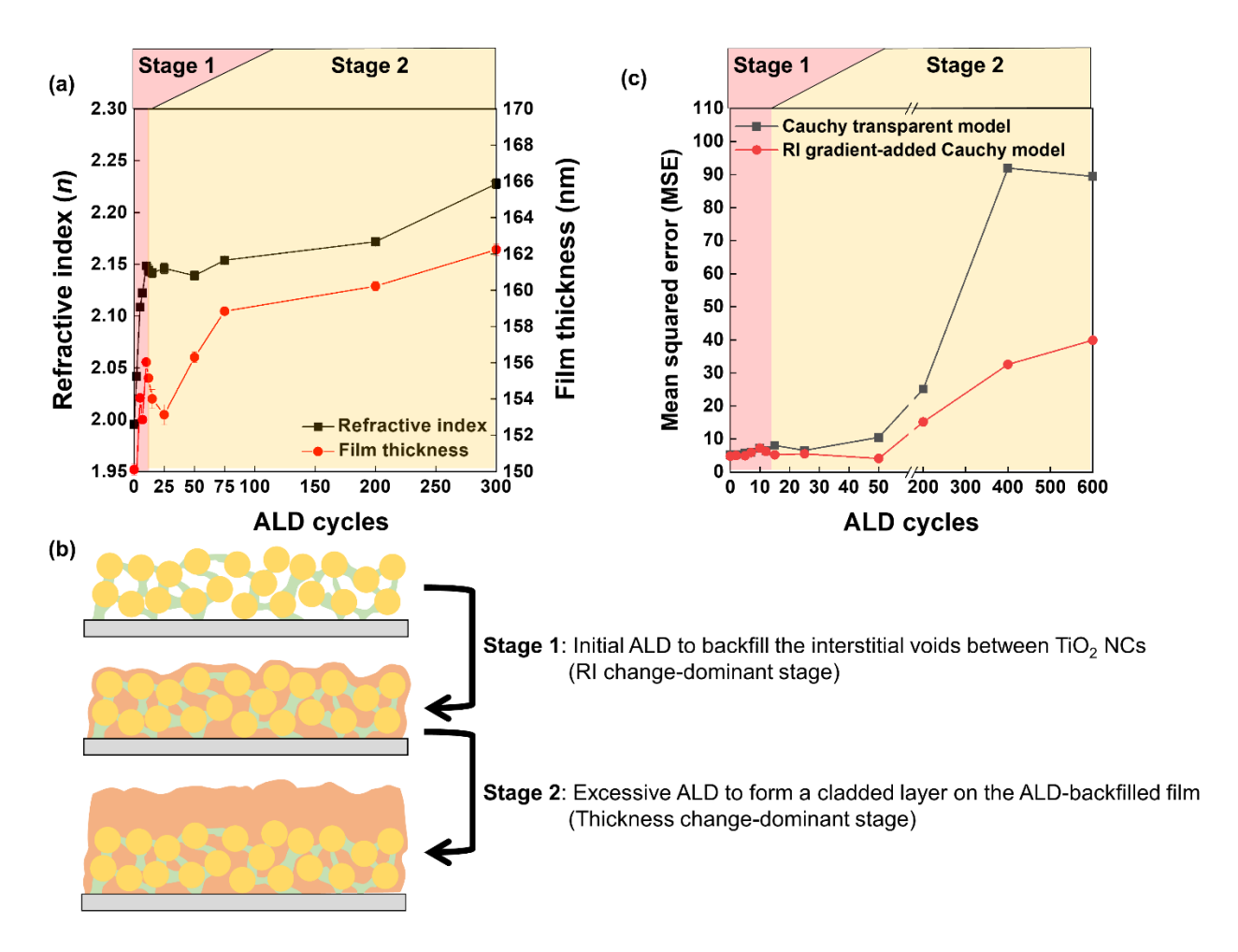


Figure 1. (a) Plots of the refractive index (RI) and film thickness of the calcined TiO₂ nanocrystal-based planar films versus ALD cycles (using an RI gradient-added Cauchy model) and (c) the mean squared errors (MSEs) obtained during the ellipsometric measurement using the ideal Cauchy transparent model in comparison with its RI gradient-added model. (b) Schematic illustration of a two-stage ALD process onto and within the porous TiO₂ nanocrystal-based film.

The RI gradient model can be used to estimate the RI values at the top and bottom of the film. Figure 2 shows the results of the model for the indicated cycles of ALD. Prior to ALD (Figure 2a) and following 12 cycles of ALD (Figure 2b), an RI difference between top and bottom is small, indicating a uniform deposition of ALD precursors throughout the film as illustrated in Figure 1b.

After 15 cycles, however, a physically meaningful RI gradient in the model (*ca.* 0.05) is discernable (Figure 2c) with a slightly higher index at the top of the film. As ALD cycles increase, this gradient gets larger due to the deposition of a cladding layer on the backfilled film surface, and the film after 200 cycles (Figure 2d) and the model indicate a more significant RI differential (*ca.* 0.15). Figure 2e summarizes the trend of the RI gradient increase in terms of ALD cycles. The RI at the bottom remains nearly constant for all the films, whereas the value at the top surface gradually increases. An ALD-deposited TiO₂ film is known to yield an RI in the range of 2.5-2.6 at this deposition temperature of 250°C, ²⁶⁻²⁷ which is higher than the RI of the ALD-backfilled TiO₂ film which is approximately 2.15. Hence, it is reasonable to observe this gradual RI increase on the surface once ALD forms a cladding layer.

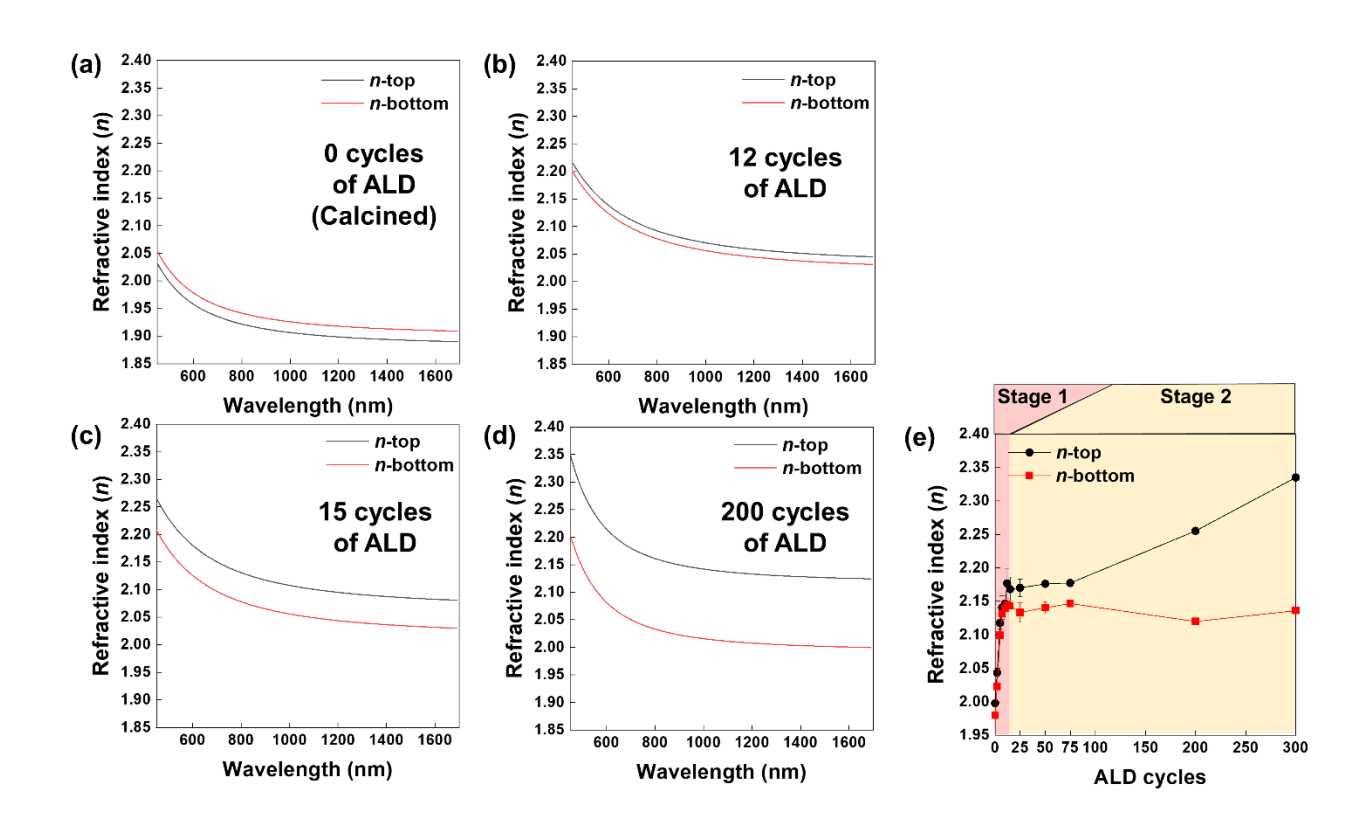


Figure 2. The refractive index (RI) graphs of the calcined TiO₂ nanocrystal-based planar films modelled by the Cauchy transparent model with an RI gradient function showing two different graphs at the top and bottom of the films after different cycles of ALD at 250°C: (a) 0 cycles, (b) 12 cycles, (c) 15 cycles, and (d) 200 cycles. (e) The variations of RIs at the wavelength of 543 nm at the top and bottom versus ALD cycles. The small RI gradients in (a) and (b) are not physically meaningful and not present in the films since the mean squared error (MSE) remained the same after adding the RI gradient function to the Cauchy transparent model.

The VASE analysis confirms that the ALD precursor of TiO₂ can diffuse throughout the thickness of the film, at least up to the film thickness range examined (*ca.* 150 nm). A thicker film of *ca.* 250 nm was also investigated and followed the same trend, which in turn means that this ALD backfill and accompanying increase in RI can be applied to at least a half micron feature dimension, considering the fact that the diffusion of the ALD precursor takes place from all directions into the patterned structures.

The experimental result that the first backfill stage was mostly done over 10 cycles of TiO₂ ALD gives a rough estimation of the average pore size in the range of 1.5-2 nm for the calcined TiO₂ NC-based film based on the growth rate of ALD at 250°C (~0.05 nm/cycle)²⁶⁻²⁷ and the kinetic diameter of the tetrakis(dimethylamino)titanium (TDMAT) ALD precursor (~0.7 nm)²⁸⁻³⁰.

Assessment of TiO₂ NC-based films

The quality of all-inorganic TiO₂ films is evaluated by SEM (Figure 3) and AFM (Figure 4). Three films of different RIs are compared: a calcined film (0 cycle), a partially backfilled film (5 cycles), and a fully backfilled film (15 cycles). 15 cycles of ALD will be used as an optimized

number of ALD cycles hereafter to ensure the complete backfill of the porosity although 10 cycles seemed sufficient. Figure 3 shows the top-down and cross-sectional SEM images of the films. Irrespective of ALD cycles, they all give smooth surfaces and cross sections. With a closer look at the cross sections, it could be said that surface roughness seems to be slightly reduced after the ALD backfill process. In Figure 4, the RMS roughness measured by AFM confirms that the films are smooth and of high quality. The measured quantitative decrease in roughness from 0.44 to 0.40 nm after ALD is in line with the qualitative observation by SEM, even though it is a small change and likely within the error of the measurements. Nonetheless, it is clear that surface roughness is not adversely impacted by ALD. Any smoothening effect resulting from ALD would be advantageous when it comes to imprinting optical elements whose side wall roughness is important. The effects of roughness on scattering losses and the resultant degradation of optical performance have been well studied for optical components such as lenses, gratings, and waveguides. The roughness of the films studied here will not contribute significantly to such losses.

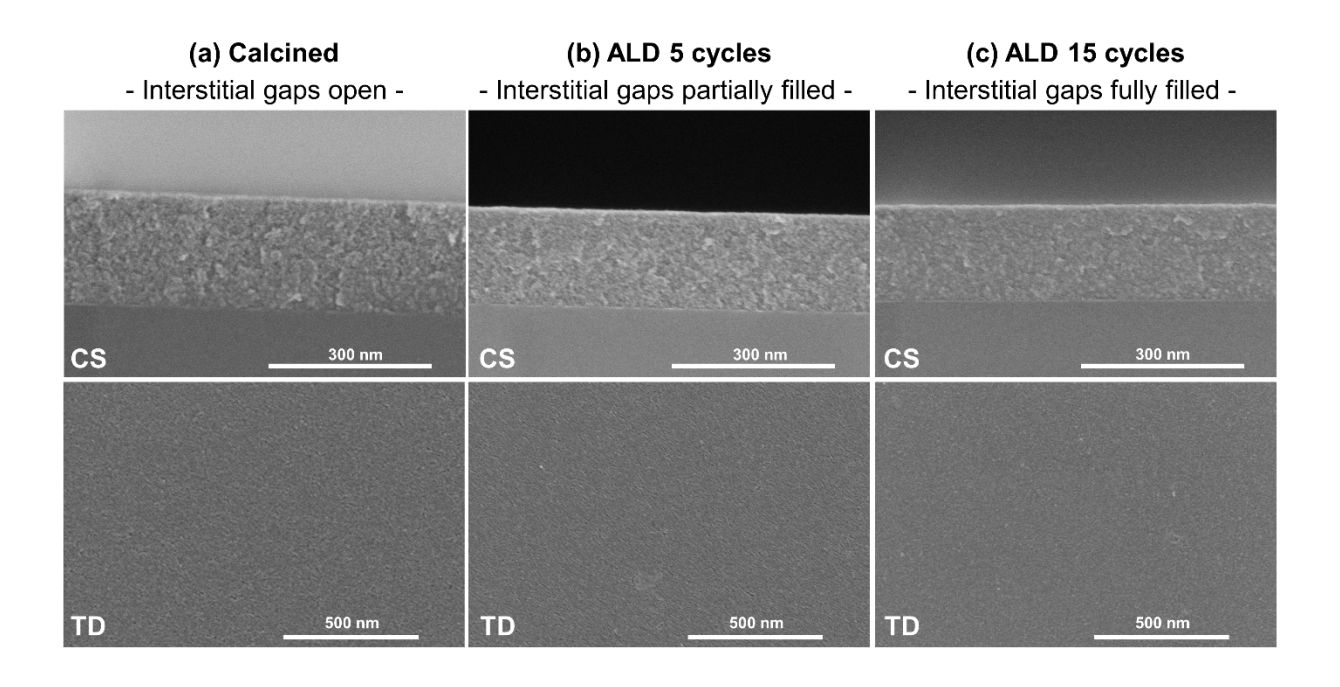


Figure 3. The top-down (TD) and cross-sectional (CS) SEM images of the TiO₂ nanocrystal-based planar films after (a) the calcination at 500°C followed by ALD at 250°C for (b) 5 cycles and (c) 15 cycles.

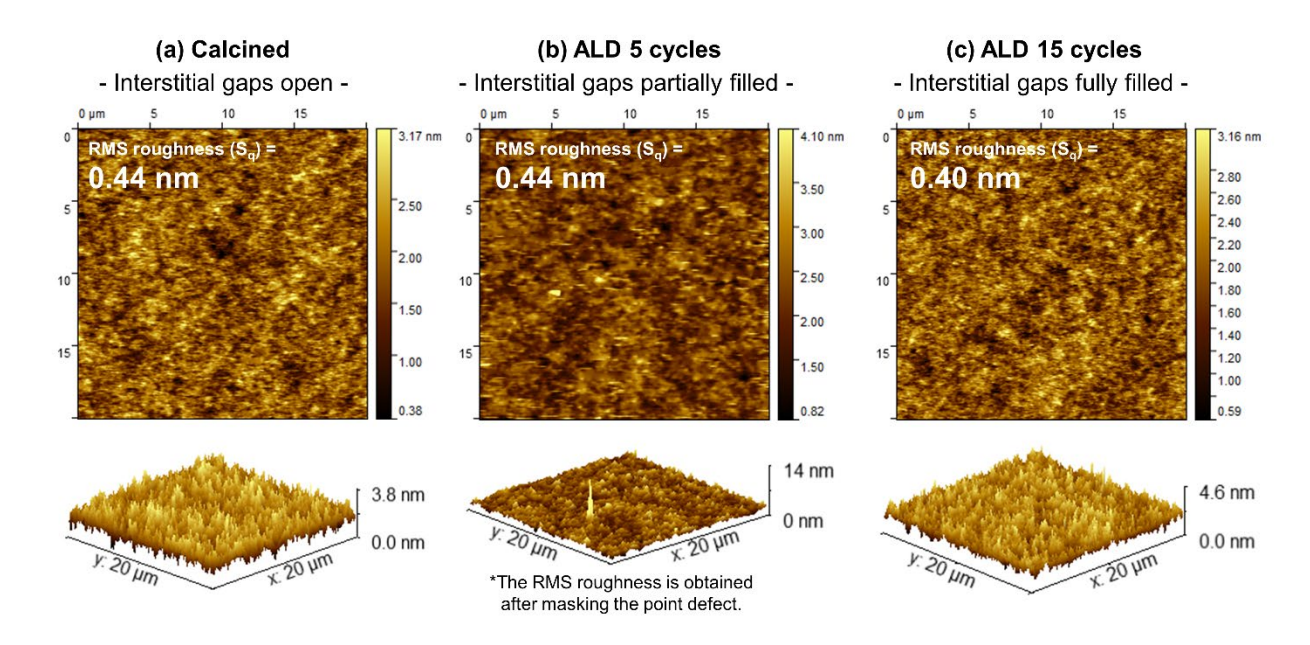


Figure 4. The AFM analysis of the TiO₂ nanocrystal-based planar films after (a) the calcination at 500°C followed by ALD at 250°C for (b) 5 cycles and (c) 15 cycles.

Figure 5 shows the FIB/TEM images of three different films. The calcined (0 cycle), the uniformly backfilled film (15 cycles), and a cladded film (400 cycles) are investigated. The TEM analysis indicates that the NC packing is uniform throughout the film and that ALD backfilling does not lead to heterogeneities. Figure 5 verifies the uniform packing of NCs from top to bottom. The ALD backfill appears to be uniform, however, this observation is difficult to quantitate even by FIB/TEM since the thickness of the backfilled ALD layer within the porous structure is as small as 0.5 nm from the surface of each NC. Nonetheless, the images (Figure 5a vs 5b) indicate that there are no obvious heterogeneities introduced by the ALD process and the contrast between the crystalline NCs and their interstitial regions appears to diminish after 15 cycles of ALD, which is

consistent with filling of voids between NCs by ALD. The thinnest measurable lamella was prepared to observe the contrast change by backfilling, but the small average NC size of 8 nm is limiting as it is on the order of the thinnest lamella. The TEM images also verify the presence of the anatase crystalline phase of NCs as expected. The cladded layer by ALD in Figure 5c is also composed of crystalline phases. A magnified image of Figure 5c is available in Figure S1 to clearly show the presence of crystalline phases. The anatase phase has been reported to be formed at ALD deposition temperatures of 250°C while amorphous TiO₂ is known to be formed below 200°C.²⁶⁻²⁷ At temperatures yielding crystalline phases of TiO₂, it is well known that a minimum number of ALD cycles (deposited film thickness) is required to obtain the crystalline phase.³⁵ The minimum film thickness is surpassed using the number of cycles for deposition of the cladding in this study.

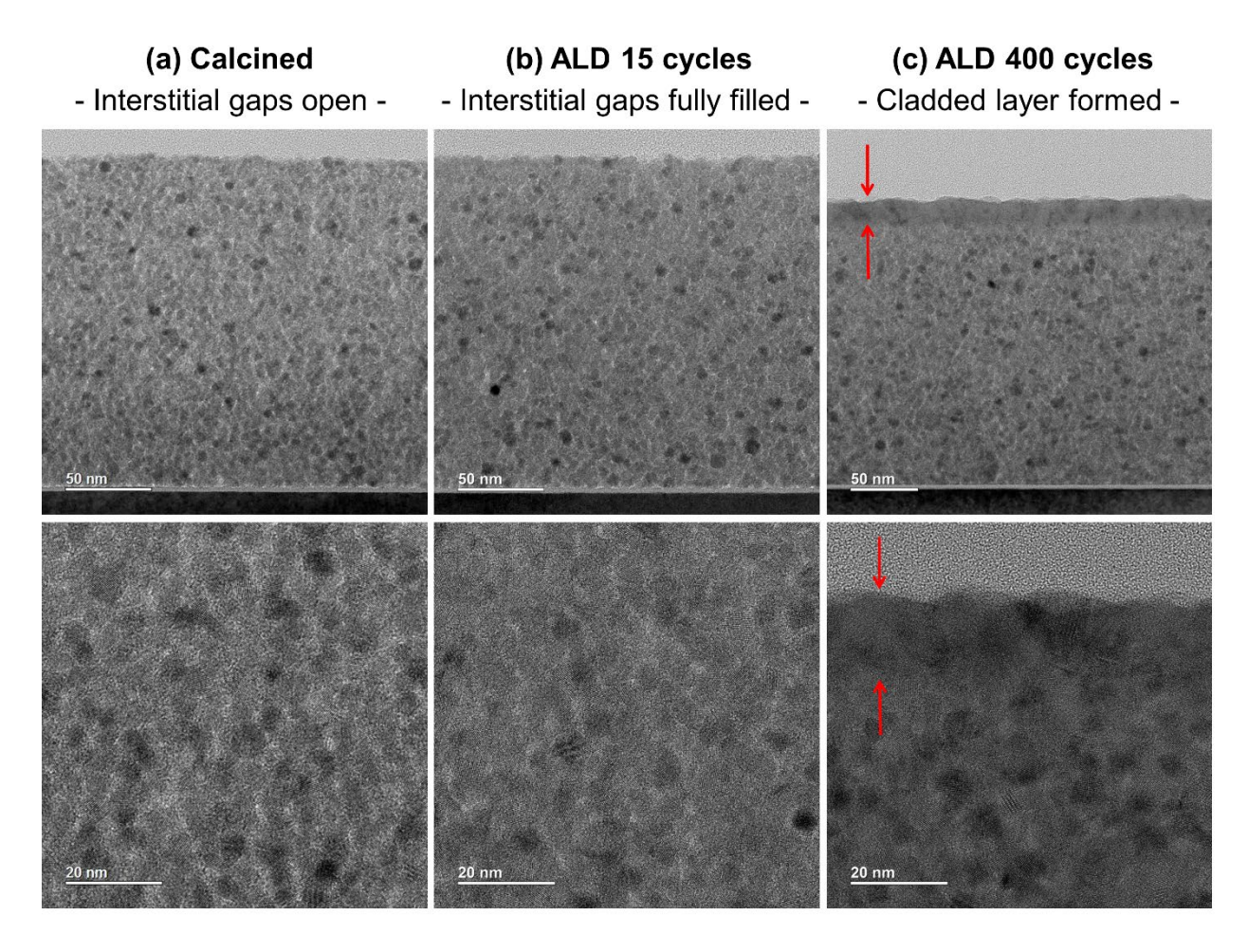


Figure 5. The FIB/TEM images of the TiO₂ nanocrystal-based planar films after (a) the calcination at 500°C followed by ALD at 250°C for (b) 15 cycles and (c) 400 cycles.

Applications of ALD onto patterned nanostructures

The practical applications of the all-inorganic TiO₂ structure and its RI tuning by ALD in the field of advanced optics are demonstrated by a single-step, direct NIL process. Figure 6 shows imprints replicated from a master mold with a binary 500 nm line pattern using a PDMS-based elastomeric stamp as described in Scheme 1a. The post-treatments including calcination and ALD onto the imprints are followed. The uniformity of imprints after the post-treatments is investigated by SEM/EDX analysis although ellipsometry was still applicable by targeting the planar area of

the imprints and the same trend as observed in the planar films was observed. To better track the homogeneous diffusion of the ALD precursor and its deposition within the porous NC film, Al₂O₃ was employed instead of TiO₂ in order to provide elemental contrast for EDX analysis. This strategy was successful in deconvoluting EDX signals between TiO₂ NCs and ALD-deposited Al₂O₃ films, which simulates the diffusion behavior of the TiO₂ ALD precursor. As shown in Figure 6, the ALD of Al₂O₃ experiment was designed in three different ways. The first TiO₂ imprint (Figure 6a) was backfilled by Al₂O₃ with just 2 cycles to show the uniform deposition in the early stage of ALD throughout the patterned nanostructures. The second TiO₂ imprint (Figure 6b) was backfilled and cladded by excessive cycles (200 cycles) of Al₂O₃ ALD, which is designed to show the formation of the cladded layer as well as to confirm the uniformity of the backfill process. In the last TiO₂ imprint (Figure 6c), both ALD precursors of TiO₂ and Al₂O₃ were utilized. 15 cycles of TiO₂ and 185 cycles of Al₂O₃ were carried out for the backfill process and the cladding process, respectively, which is different from the second sample in that the backfill process was done by TiO₂, not by Al₂O₃.

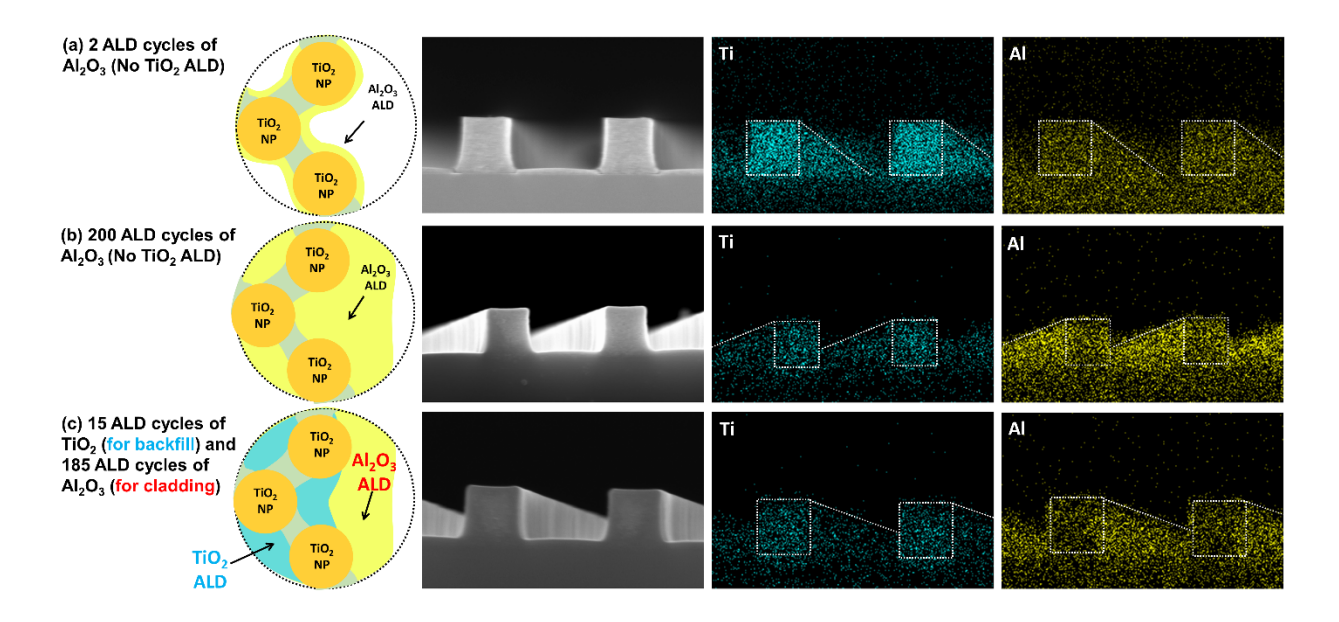


Figure 6. The SEM/EDX analysis of the imprinted 500 nm line patterns using a TiO₂ nanocrystal-based ink and the single-step direct nanoimprint lithography focused on the signals from Ti and Al atoms together with illustrations showing an expected ALD process of Al₂O₃ or TiO₂ onto the patterned TiO₂ structures with porosity after (a) 2 cycles of Al₂O₃, (b) 200 cycles of Al₂O₃, or (c) 15 cycles of TiO₂ followed by 185 cycles of Al₂O₃. The samples were cleaved to image cross-sections after the completion of all ALD processes.

The comparison of the three different imprints in Figure 6 confirms the feasibility of using ALD for RI tuning of nanocrystal-based imprints. In Figure 6a, almost the same intensity of Al signals throughout the features and their sidewalls verifies the uniform deposition of ALD precursors. In Figure 6b, the stronger and denser signals of Al on the sidewalls compared to those within the cross-sectioned features are indicative of the formation of a cladded layer by Al₂O₃. By comparison, the signals for Ti are more intense within the features because the sidewalls are covered and obscured by the Al₂O₃ layer. In the last sample whose backfill process was done by TiO₂ instead of Al₂O₃, the frequency of Al signals within the features seems to be further reduced because very limited porosity remains for the Al₂O₃ deposition after TiO₂ ALD within the pores. In Figure S2, the cladded layer of Al₂O₃ can be clearly seen by SEM at a higher magnification.

Fabrication of all-inorganic TiO₂ metalenses

More complex nanostructures are fabricated with the TiO₂ NC-based ink and the post-processing. A large-scale fabrication of an array of 4-mm-diameter metalenses, which are composed of nanoposts, is an excellent proof-of-concept tool to show the practical importance of RI tuning. Figure 7 shows the SEM and FIB/TEM images of a 4-mm-diameter metalens imprint

consisting of a myriad of circular nanoposts with varying diameters and aspect ratios. In the SEM images, all the densely arranged nanoposts are successfully replicated from the metalens master without any major breakage or loss of features. Additional SEM images of the imprint are available in Figure S3 and the images of the master are also available in Figure S4 for comparison. Feature dimensions as small as 80 nm and aspect ratios up to 8.3 are achieved. The TEM images show that the packing of TiO₂ NCs in the metalens imprint is uniform and comparable to that observed in the planar films although different fluid dynamics are present due to solvent uptake of elastomeric stamp and capillary action into the patterned structures. The crystalline phase of NCs is also confirmed. The darker areas around the sidewalls did not result from the non-uniformity of the packing but rather from the preparation of the FIB/TEM sample. Because the sidewalls of the metalens are not perfectly vertical (in both master and imprint) and the diameter of the posts varies across the lens, the lamella sectioning was misaligned with the posts' centers.

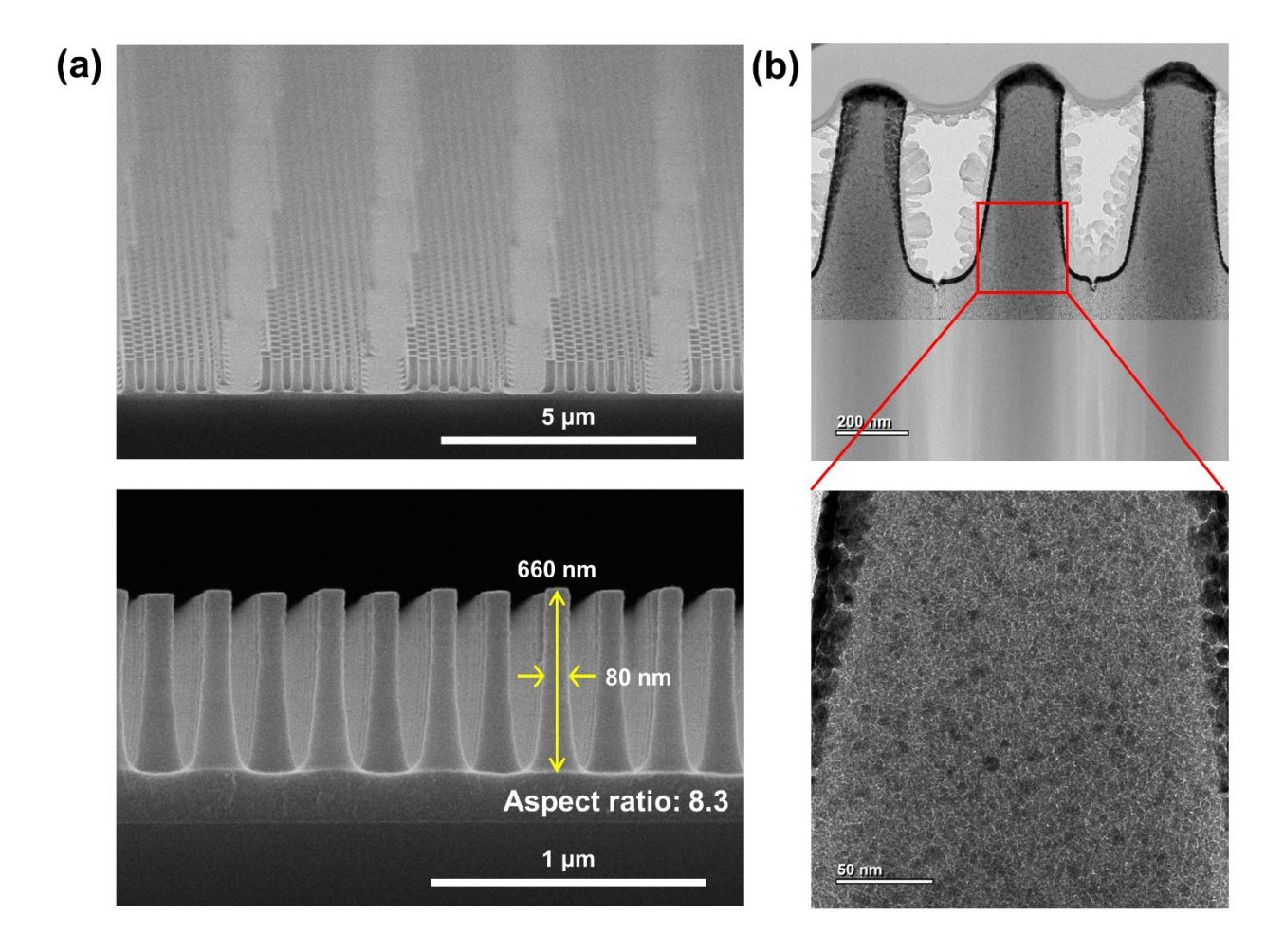


Figure 7. (a) The cross-sectional SEM and (b) FIB/TEM images of an imprint replicated from a 4-mm-diameter metalens master using a TiO₂ nanocrystal-based ink and the single-step direct nanoimprint lithography before calcination and ALD.

Figure 8 shows the optical performance of the array of twelve 4-mm-diameter metalenses including focusing efficiencies and focal spot images before the post-treatments. As shown in Figure 8b, a metalens imprint was fabricated on a transparent fused silica substrate to test the optical performance. 12 lenses out of 30 lenses on the master design (Figure 8a) were optically tested since the lenses closest to the edge of the master could not be successfully replicated because of the edge effect from the manual stamp making and manual imprinting processes. As shown in

Figure 8c, five columns in the array are labeled by +20 nm, +10 nm, 0 nm, -10 nm, and -20 nm. The metalenses in each column have the same designs, and different columns are generated by increasing or decreasing all nanopost diameters of a base design, which is labeled 0 nm, by the labeled amount (see Materials and Methods for more details). The metalenses in three different columns (+10 nm, +0 nm, -10 nm) were tested and averaged and their focusing efficiency values are reported in Figure 8d. The average and standard deviation of the focusing efficiencies of the tested 12 lenses are 60.9% and 3.3%, respectively. The standard deviation of efficiencies of the 12 lenses is similar to that of efficiencies in the same column, suggesting that the efficiency variations are more related to the inconsistency of imprinting quality than the ± 10 nm diameter change included in the design. The imprint inconsistency was expected since the imprint process was performed manually. Nonetheless, the efficiency average of 61% is higher than the 43% and 57% values respectively reported for 4-mm-diameter and 400-μm-diameter metalenses in our recent work.¹⁷ The simulated efficiencies of the +10 nm, 0 nm, and -10 nm biased metalenses were 70.5%, 66.2%, and 61.0%, respectively. The experimentally determined efficiencies of the corresponding designs are quite close to the simulated values if the highest efficiency of each design is compared: 66.9% vs 70.5% (+10 nm); 65.0% vs 66.2% (0 nm); 59.9% vs 61.0% (-10 nm). Figure 8d also shows nearly diffraction-limited circular and symmetric focal spots for all the lenses except for some lenses close to the edge of the imprint such as R5C3 and R5C4.

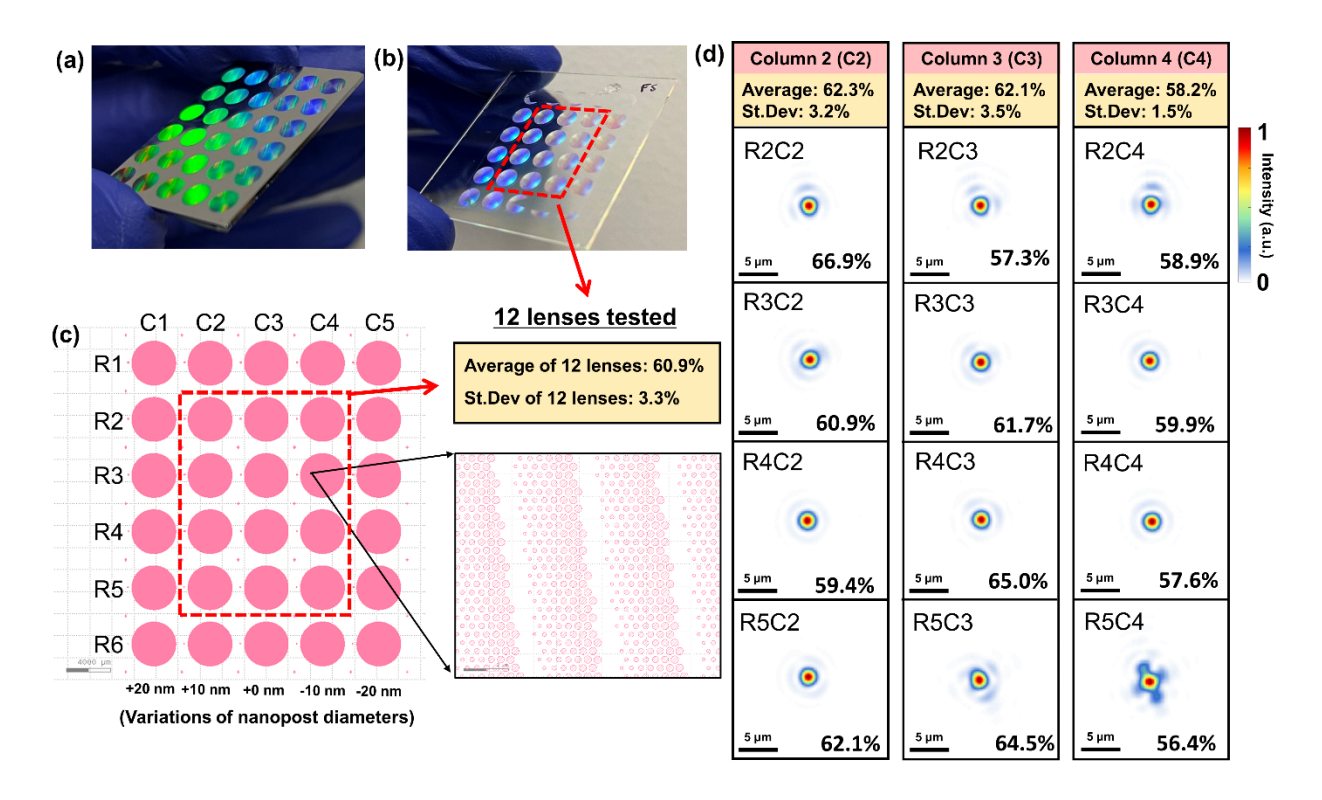


Figure 8. The pictures of (a) the metalens master mold and (b) an imprint including an array of 4-mm-diameter metalenses fabricated on a fused silica substrate. (c) The master has five different designs of metalenses with different nanopost diameters (+20, +10, +0, -10, -20 nm) and three of them (+10, +0, -10 nm) are successfully replicated and optically characterized. (d) The focusing efficiencies and focal spot images of the 12 lenses in the imprint from the three different designs at the target wavelength of 543 nm. The efficiency of each lens is determined by the ratio of the optical power focused by the lens to the optical power incident on the lens aperture. Some lenses close to the edge such as R5C4 show a non-circular or asymmetric focal spot because of edge effects. The simulated efficiencies were 70.5%, 66.2%, and 61.0% for the +10 nm, 0 nm, and -10 nm biased metalenses, respectively.

Effects of RI tuning on the metalens performance

The effects of the post-fabrication ALD process and its RI tuning on the optical performance of the metalenses are investigated by tracking the change of efficiencies of the lenses throughout the post-imprint treatments including calcination and ALD. The R2C2 lens, which has the highest efficiency (see Figure 8), and three lenses (R3C3, R4C3, R5C3) from the base design (column 3, 0 nm) are tracked. Figure 9a shows that the calcination and ALD increase the focusing efficiency of all the lenses. The efficiency of the best performing (R2C2) lens increased by 8% and reached 75% with just 15 cycles of TiO₂ ALD, which is comparable with metalenses fabricated by subtractive manufacturing method.³⁶ The focal spot images of the lenses remain similarly symmetric and nearly diffraction-limited after the post-treatments. In Figure S5, the efficiencies and focal spot images of the rest of the lenses are given. The average efficiency of the post-treated lenses is 67% which is 6% higher than the average before calcination and ALD shown in Figure 8. This efficiency increase is ascribed to the RI increase during the calcination and ALD postfabrication steps since the RI change of the material comprising the nanoposts, also known as meta-atoms in the meta-surface, is directly related to the diffraction efficiency of the meta-atom arrays. Meta-atoms with a higher RI after ALD can diffract light passing through them more efficiently and provide a diffraction-limited focusing.

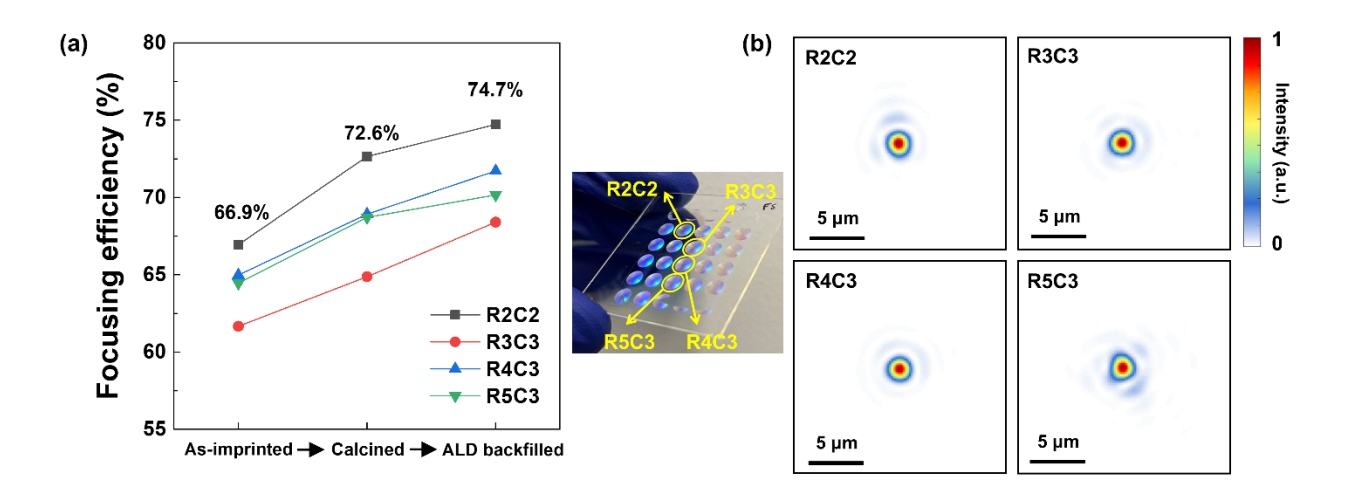


Figure 9. (a) The focusing efficiencies of R2C2, R3C3, R4C3, and R5C3 lenses (also shown in Figure 8) throughout post-treatments including calcination and 15 cycles of TiO₂ ALD and (b) the focal spot images of the lenses after the post-treatments.

Conclusions

A method for providing high RI metal oxide nanostructures, not limited to TiO₂, was demonstrated by combining a small number of ALD cycle with direct patterning of NC-based inks through solvent-assisted NIL that is fast and scalable. The RI of NC-based films can be increased quickly through post-processing ALD. After just 15 cycles of ALD, the RI increased from 2.00 to 2.15. HAR TiO₂ pillars across the 4-mm-diameter metalenses were successfully fabricated and densified by ALD, yielding focusing efficiencies up to 75% which is larger than 90% of the efficiency of the target design (82%). Not only is this method of interest for enhancing optical properties by increasing RI, it also introduces a versatile method for fabricating complex nanostructures by designing new stamp patterns as well as fabricating materials with varied compositions, as we have demonstrated by ALD of Al₂O₃ onto TiO₂ NC-based structures. Additional cycles of ALD can also be utilized in some cases as a path to tune the feature dimensions of the patterned nanostructures or to match the master design in a single ALD run.

Materials and Methods

Materials

All materials were purchased from Sigma Aldrich and used as received without further purification unless specified. 50 wt% titanium dioxide (TiO₂) nanocrystals dispersed in propylene glycol monomethyl ether acetate (PGMEA) were purchased from Pixelligent Technologies, LLC.

Preparation of TiO₂ NC-based inks

A 22 wt% TiO₂ nanocrystal-based ink was prepared by diluting with a solvent mixture of ethyl lactate (EL) and 2-(2-butoxyethoxy)ethyl acetate (which contains a 0.15 wt% of an anionic surfactant relative to EL) and a silane coupling agent was then added to the concentration of 15 wt% relative to the mass of TiO₂ NCs. After mixing all the components, the TiO₂ NC-based ink was sonicated for at least 10 minutes.

Stamp making

A two-layered stamp composed of hard PDMS (h-PDMS) and soft PDMS (s-PDMS) was fabricated. To make the first h-PDMS layer, 1.7 g of 7-8% vinyl methylsiloxane-dimethylsiloxane (Gelest, Inc.), 5 μL of 2,4,6,8-tetramethyl-2,4,6,8 tetravinylcyclotetrasiloxane, 9 μL of platinum-divinyltetramethyl disiloxane (Gelest, Inc.), and 5 g of toluene were mixed vigorously and then 0.5 mL of 25-30% methylhydrosiloxane-dimethylsiloxane (Gelest, Inc.) was added and mixed again. The mixture was spin-coated onto the Si master mold (3000 rpm, 40 seconds, 1500 rpm/s ramp rate). Then, the spin-coated master was cured at 100°C for 45 minutes. The master was removed from the oven and cooled to room temperature before depositing the second s-PDMS

layer, Sylgard 184 (Dow Corning), whose mixture (10:1 wt% ratio) was degassed under vacuum prior to the lamination with the h-PDMS layer. The second s-PDMS layer was poured onto a 0.2 mm-thickness glass backing (Howard glass) pre-treated with 1,1,1,3,3,3-hexamethyldisilazane (HMDS, Acros Organics) to make a better stamp adhesion to the glass, and the stamp thickness was controlled by placing four footers at each corner of the master. The h-PDMS coated Si master was slowly placed onto the drop-cast Sylgard with the patterned side facing down and gently pressed until the desired thickness limited by the footers was achieved. The assembly on the glass backing was cured in a 75°C oven overnight. The assembly was allowed to cool to room temperature after curing and the master was demolded from the h-PDMS/s-PDMS stamp with the aid of isopropyl alcohol (IPA) lubrication. The stamp was rinsed immediately with IPA and water to prevent any feature collapse by rapid IPA drying. The master was also cleaned with IPA for the next stamp making process.

Fabrication of TiO₂ NC-based planar films and imprints

All the fabrication steps described here were done in general lab space, except for the ALD process which was done in the cleanroom. TiO₂ NC-based planar films and imprints were fabricated onto Si (University Wafers) or fused silica (Precision Micro-Optics) substrates. The substrates were cleaned with UV/Ozone (a UVO 342 from Jelight Company Inc.) for 10 minutes right before imprinting. The 22 wt% TiO₂ NC-based ink was deposited onto a substrate and spin coated (2000 rpm, 30 seconds, 1500 rpm/s ramp rate). To make a planar film, the spin-coated film was baked at 100°C for 30 seconds to remove some excess solvents which prevented a dense packing of TiO₂ nanocrystals during the following UV curing step. Once the film was cooled to room temperature, which took about a minute, the film was cured and solidified by UV. In the case

of imprinting with an h-DPMS/s-PDMS stamp, baking was not required since contact with the elastomeric stamp played a similar role by absorbing solvents and densifying the structures. The assembly was transferred to the UV stage and cured. The UV curing was all done with a custom-made UV tool (Carpe Diem Technologies) which can generate a pulsed UV source at 365 nm (35 V, pulse on for 5 milliseconds, pulse off for 15 milliseconds, 4,000 repetitions of the pulses). The overall curing time of the pulsed UV took 80 seconds. Once the imprint was cured, the stamp can be released very slowly from one edge to the other edge and it can be re-used for the next imprint without any cleaning process or pause time. The UV-cured planar films or imprints were calcined at 500°C for 2 hours in air atmosphere, resulting in all-inorganic TiO₂ structures. The calcined films or imprints were used for the ALD process. The overall fabrication process is also schematically described in Scheme 1a.

Atomic layer deposition (ALD)

The ALD process onto the calcined films and imprints was done at 250°C in a Cambridge NanoTech Savannah 90 Atomic Layer Deposition system. Tetrakis(dimethylamido)titanium (IV) (TDMAT) and trimethylaluminum (TMA) were used as the ALD precursors for the deposition of TiO₂ and Al₂O₃, respectively. The recipe for the TiO₂ deposition included a 0.1 second of TDMAT pulse followed by a 0.015 second of H₂O pulse and the waiting time after each pulse was 5 seconds. In the case of the imprint consisting of the array of metalenses, the recipe was modified and an extended exposure mode was introduced because of the extremely higher surface area enhancement compared to the planar films and the binary line patterns. In the extended exposure mode, the soaking time of the TiO₂ precursor into the imprint was increased to 10 seconds for both

TDMAT and H₂O pulses with the vacuum valve closed, which made the diffusion of the precursor into high aspect ratio features uniform.

Master design and fabrication

The metalens design consists of 700-nm-tall circular nanoposts with diameters ranging from 100 nm to 280 nm arranged on a triangular lattice with 430 nm lattice constant. A refractive index (RI) of 1.9 and 1.46 were assumed for the nanoposts and the fused silica substrate, respectively. The metalenses have a diameter of 4 mm and a focal length of 9.8 mm (i.e., numerical aperture of 0.2) at the design wavelength of 543 nm.

The metalens master comprises six identical rows of 4-mm-diameter metalenses etched into a silicon substrate. Within a row, the metalens patterns are varied to account for process variance: the nanopost diameters are uniformly biased from -20 nm to +20 nm in steps of 10 nm from the nominal design (i.e., 5 patterns per row). The master was fabricated by NYCreates (Albany, NY) using DUV photolithography to define the metalens patterns and plasma etching to transfer the patterns to a 775-um-thick silicon wafer. The targeted etch depth was 840 nm, to account for 17% shrinkage in post height (15% for lateral shrinkage) after imprint due to densification.

The nanoposts' dimensions on the fabricated master were measured using SEM. The nanoposts were found to be ca. 820 nm tall and the diameters of the nominal design (i.e., the 0 nm bias) found to vary between 50 nm to 275nm.

The fabricated metalens master was further cleaned with RCA-1 procedure, so-called "standard clean-1," to ensure complete removal of any residues. Deionized water (DI H₂O), ammonium hydroxide (28-30% NH₄OH), and hydrogen peroxide (30% H₂O₂) were mixed with

5:1:1 volume ratios. The mixture of DI H_2O and NH_4OH was heated on a hotplate and removed from the hotplate once it reached $70\pm5^{\circ}C$, and H_2O_2 was then added. After observation of vigorous bubble formation in 1-2 minutes, the master was soaked into the mixture for 15 minutes. The master was rinsed with overflowing water followed by IPA and dried with compressed N_2 .

Master fluorination

The fabricated Si masters were cleaned with IPA and compressed air, followed by UV/Ozone treatment for 30 minutes prior to a vapor phase fluorination. The masters were placed in a vacuum desiccator affixed with a vial containing a 0.1 mL of heptadecafluoro-1,1,2,2-tetrahydrodecyltrichlorosilane (Gelest, Inc.) and the desiccator was pumped down for 30 seconds on a Schlenk line, sealed, and left overnight at room temperature. The fluorinated masters were removed from the desiccator and rinsed with IPA, water and then IPA again to remove any unreacted material from the masters' surface.

Characterization of films and imprints

The RI measurements of planar films or a planar area of the imprints on Si wafers were taken on a JA Woollam RC2 variable angle spectroscopic ellipsometer (VASE) at five different angles between 45° and 65° with a scan interval of 5° over the wavelength range of 450-1000 nm. Ellipsometric data were fit using the Cauchy transparent thin film on Si model available in the CompleteEase software. More specifically, an advanced model of the Cauchy model was introduced by adding an RI gradient function along the height of a film. The RI values reported in the present study were all taken at the wavelength of 543 nm which was the target wavelength of the metalens design.

The SEM/EDX images of imprints were taken with a FEI Magellan 400 FESEM and their feature dimensions were measured using ImageJ software. The surface of planar films was analyzed by an Asylum Research MFP-3D atomic force microscope with tapping mode at 1 Hz over a 20 x 20 µm area. The FIB/TEM imaging was performed commercially at Covalent Metrology (Sunnyvale, CA), an analytical laboratory. During the lamella preparation, e-beam deposition of carbon was utilized to preserve nanoposts' structure and to prevent charging and local thermal heating that could affect the crystalline nature of the films.

Optical testing of metalenses

The optical performance of the metalenses including focusing efficiencies and focal spot images was tested using a Uniphase JDSU 1676 HeNe laser source with unpolarized collimated beam operating at the wavelength of 543 nm as described in our recent publication. A laser beam expander (Melles Griot 10X) was used to provide a large incident beam with planar phase front at the lens's surface and a 4-mm-diameter aperture was placed right before the lens to ensure the same beam size incident on the lens. The focal spot image of a lens was captured by a CCD with a 50x objective lens and a tube lens (focal length: 20 cm).

The focusing efficiency of a metalens is the ratio (P/P_0) of the optical power focused by the metalens (P) to the optical power incident on it (P_0) . Because of the long focal length of the 4-mm-diameter metalens, the power focused by the lens (P) was measured at the real focal plane. The incident laser beam was partially focused using a 5 cm focal length lens to ensure all the laser power passed through the metalens aperture. The light focused by the metalens was measured by a power meter (ILX Lightwave OMM-6810B with an OMH-6722 power head) with a 40- μ m-diameter pinhole placed at the focal spot. The power incident on the metalens (P_0) was

determined by measuring the power collected at the power meter when the metalens and the 40 µm pinhole were removed and taking Fresnel reflection into account at the air-substrate interface where 3.5% of the power was lost due to the RI change from 1.0 to 1.46. Thus, a Fresnel reflection-corrected focusing efficiency is reported in this study, which could be 2-3% higher than the absolute focusing efficiency without this correction.

Metalens simulations

The focusing efficiencies of the metalenses were estimated using the grating averaging technique.³⁷ The efficiency of the target design (RI of 1.9, 700-nm-tall nanoposts with diameters ranging from 100 nm to 280 nm) was found to be 82%. For the imprinted metalenses, we assumed an RI of 1.95 for the nano-posts, 25% dimensional shrinkage, and a 90-nm-thick residual layer due to the imprint process, and found efficiencies of 70.5%, 66.2%, and 61.0% for the +10 nm, 0 nm, and -10 nm biased metalenses, respectively.

Supporting Information

Additional characterization, supplementary figures. This material is available free of charge via the Internet at http://pubs.acs.org.

Supporting information: A magnified TEM image of a cladded film by ALD, additional SEM images of the line pattern cladded by Al₂O₃ ALD, the images of the metalens imprint on Si, and the images of the metalens master, and the focusing efficiencies of the ALD-backfilled metalens array

Corresponding Author

*watkins@polysci.umass.edu

Acknowledgements

This work was supported by the NSF Center for Hierarchical Manufacturing at the University of Massachusetts (CMMI-1025020), the Army Research Laboratories (HQ00341520007) and the National Science Foundation (PFI-RP 2122654).

Conflict of Interest Disclosure

JJW has a financial interest in Myrias Optics, Inc., which has licensed technology associated with imprinted optical components.

References

- 1. Kim, I.; Yoon, G.; Jang, J.; Genevet, P.; Nam, K. T.; Rho, J., Outfitting Next Generation Displays with Optical Metasurfaces. ACS Photonics 2018, 5 (10), 3876-3895.
- 2. Avayu, O.; Almeida, E.; Prior, Y.; Ellenbogen, T., Composite functional metasurfaces for multispectral achromatic optics. Nature Communications 2017, 8 (1), 14992.
- 3. Khorasaninejad, M.; Chen, W. T.; Devlin, R. C.; Oh, J.; Zhu, A. Y.; Capasso, F., Metalenses at visible wavelengths: Diffraction-limited focusing and subwavelength resolution imaging. Science 2016, 352 (6290), 1190-1194.
- 4. Kumar, K.; Duan, H.; Hegde, R. S.; Koh, S. C. W.; Wei, J. N.; Yang, J. K. W., Printing colour at the optical diffraction limit. Nature Nanotechnology 2012, 7 (9), 557-561.
- 5. Lee, G.-Y.; Yoon, G.; Lee, S.-Y.; Yun, H.; Cho, J.; Lee, K.; Kim, H.; Rho, J.; Lee, B., Complete amplitude and phase control of light using broadband holographic metasurfaces. Nanoscale 2018, 10 (9), 4237-4245.
- 6. Staude, I.; Miroshnichenko, A. E.; Decker, M.; Fofang, N. T.; Liu, S.; Gonzales, E.; Dominguez, J.; Luk, T. S.; Neshev, D. N.; Brener, I.; Kivshar, Y., Tailoring Directional Scattering through Magnetic and Electric Resonances in Subwavelength Silicon Nanodisks. ACS Nano 2013, 7 (9), 7824-7832.
- 7. Yoon, G.; Lee, D.; Nam, K. T.; Rho, J., Pragmatic Metasurface Hologram at Visible Wavelength: The Balance between Diffraction Efficiency and Fabrication Compatibility. ACS Photonics 2018, 5 (5), 1643-1647.

- 8. Kress, B. C.; Chatterjee, I., Waveguide combiners for mixed reality headsets: a nanophotonics design perspective. Nanophotonics 2021, 10 (1), 41-74.
- 9. Hultqvist, A.; Edoff, M.; Törndahl, T., Evaluation of Zn-Sn-O buffer layers for CuIn0.5Ga0.5Se2 solar cells. Progress in Photovoltaics: Research and Applications 2011, 19 (4), 478-481.
- 10. Kosola, A.; Putkonen, M.; Johansson, L.-S.; Niinistö, L., Effect of annealing in processing of strontium titanate thin films by ALD. Applied Surface Science 2003, 211 (1), 102-112.
- 11. Pore, V.; Hatanpää, T.; Ritala, M.; Leskelä, M., Atomic Layer Deposition of Metal Tellurides and Selenides Using Alkylsilyl Compounds of Tellurium and Selenium. Journal of the American Chemical Society 2009, 131 (10), 3478-3480.
- 12. Johnson, R. W.; Hultqvist, A.; Bent, S. F., A brief review of atomic layer deposition: from fundamentals to applications. Materials Today 2014, 17 (5), 236-246.
- 13. Cremers, V.; Puurunen, R. L.; Dendooven, J., Conformality in atomic layer deposition: Current status overview of analysis and modelling. Applied Physics Reviews 2019, 6 (2), 021302.
- 14. Kapilashrami, M.; Kronawitter, C. X.; Törndahl, T.; Lindahl, J.; Hultqvist, A.; Wang, W.-C.; Chang, C.-L.; Mao, S. S.; Guo, J., Soft X-ray characterization of Zn1–xSnxOy electronic structure for thin film photovoltaics. Physical Chemistry Chemical Physics 2012, 14 (29), 10154-10159.
- 15. Beckel, D.; Bieberle-Hütter, A.; Harvey, A.; Infortuna, A.; Muecke, U. P.; Prestat, M.; Rupp, J. L. M.; Gauckler, L. J., Thin films for micro solid oxide fuel cells. Journal of Power Sources 2007, 173 (1), 325-345.

- 16. Huang, H.; Nakamura, M.; Su, P.; Fasching, R.; Saito, Y.; Prinz, F. B., High-Performance Ultrathin Solid Oxide Fuel Cells for Low-Temperature Operation. Journal of The Electrochemical Society 2007, 154 (1), B20.
- 17. Einck, V. J.; Torfeh, M.; McClung, A.; Jung, D. E.; Mansouree, M.; Arbabi, A.; Watkins, J. J., Scalable Nanoimprint Lithography Process for Manufacturing Visible Metasurfaces Composed of High Aspect Ratio TiO2 Meta-Atoms. ACS Photonics 2021, 8 (8), 2400-2409.
- 18. Beaulieu, M. R.; Hendricks, N. R.; Watkins, J. J., Large-Area Printing of Optical Gratings and 3D Photonic Crystals Using Solution-Processable Nanoparticle/Polymer Composites. ACS Photonics 2014, 1 (9), 799-805.
- 19. Dundar Arisoy, F.; Kolewe, K. W.; Homyak, B.; Kurtz, I. S.; Schiffman, J. D.; Watkins, J. J., Bioinspired Photocatalytic Shark-Skin Surfaces with Antibacterial and Antifouling Activity via Nanoimprint Lithography. ACS Applied Materials & Interfaces 2018, 10 (23), 20055-20063.
- 20. Howell, I. R.; Giroire, B.; Garcia, A.; Li, S.; Aymonier, C.; Watkins, J. J., Fabrication of plasmonic TiN nanostructures by nitridation of nanoimprinted TiO2 nanoparticles. Journal of Materials Chemistry C 2018, 6 (6), 1399-1406.
- 21. Kothari, R.; Beaulieu, M. R.; Hendricks, N. R.; Li, S.; Watkins, J. J., Direct Patterning of Robust One-Dimensional, Two-Dimensional, and Three-Dimensional Crystalline Metal Oxide Nanostructures Using Imprint Lithography and Nanoparticle Dispersion Inks. Chemistry of Materials 2017, 29 (9), 3908-3918.
- 22. Li, S.; Kazemi-Moridani, A.; Zhou, Y.; Howell, I. R.; Kothari, R.; Lee, J.-H.; Watkins, J. J., Wavelength-Selective Three-Dimensional Thermal Emitters via Imprint Lithography and Conformal Metallization. ACS Applied Materials & Interfaces 2018, 10 (9), 8173-8179.

- 23. Li, W.; Christiansen, T. L.; Li, C.; Zhou, Y.; Fei, H.; Mamakhel, A.; Iversen, B. B.; Watkins, J. J., High-power lithium-ion microbatteries from imprinted 3D electrodes of sub-10 nm LiMn2O4/Li4Ti5O12 nanocrystals and a copolymer gel electrolyte. Nano Energy 2018, 52, 431-440.
- 24. Li, W.; Zhou, Y.; Howell, I. R.; Gai, Y.; Naik, A. R.; Li, S.; Carter, K. R.; Watkins, J. J., Direct Imprinting of Scalable, High-Performance Woodpile Electrodes for Three-Dimensional Lithium-Ion Nanobatteries. ACS Applied Materials & Interfaces 2018, 10 (6), 5447-5454.
- 25. Zhou, Y.; Uzun, S. D.; Watkins, N. J.; Li, S.; Li, W.; Briseno, A. L.; Carter, K. R.; Watkins, J. J., Three-Dimensional CeO2 Woodpile Nanostructures To Enhance Performance of Enzymatic Glucose Biosensors. ACS Applied Materials & Interfaces 2019, 11 (2), 1821-1828.
- 26. Aarik, J.; Aidla, A.; Kiisler, A.-A.; Uustare, T.; Sammelselg, V., Effect of crystal structure on optical properties of TiO2 films grown by atomic layer deposition. Thin Solid Films 1997, 305 (1), 270-273.
- 27. Ylivaara, O. M. E.; Langner, A.; Liu, X.; Schneider, D.; Julin, J.; Arstila, K.; Sintonen, S.; Ali, S.; Lipsanen, H.; Sajavaara, T.; Hannula, S.-P.; Puurunen, R. L., Mechanical and optical properties of as-grown and thermally annealed titanium dioxide from titanium tetrachloride and water by atomic layer deposition. Thin Solid Films 2021, 732, 138758.
- 28. Dendooven, J.; Pulinthanathu Sree, S.; De Keyser, K.; Deduytsche, D.; Martens, J. A.; Ludwig, K. F.; Detavernier, C., In Situ X-ray Fluorescence Measurements During Atomic Layer Deposition: Nucleation and Growth of TiO2 on Planar Substrates and in Nanoporous Films. The Journal of Physical Chemistry C 2011, 115 (14), 6605-6610.

- 29. Detavernier, C.; Dendooven, J.; Pulinthanathu Sree, S.; Ludwig, K. F.; Martens, J. A., Tailoring nanoporous materials by atomic layer deposition. Chemical Society Reviews 2011, 40 (11), 5242-5253.
- 30. Zhou, X.; Zhao, Y.-Y.; Kim, S.-R.; Elimelech, M.; Hu, S.; Kim, J.-H., Controlled TiO2 Growth on Reverse Osmosis and Nanofiltration Membranes by Atomic Layer Deposition: Mechanisms and Potential Applications. Environmental Science & Technology 2018, 52 (24), 14311-14320.
- 31. Bennett, H. E.; Porteus, J. O., Relation Between Surface Roughness and Specular Reflectance at Normal Incidence. J. Opt. Soc. Am. 1961, 51 (2), 123-129.
- 32. Wang, K.; Liu, S.; Chen, F.; Liu, Z.; Luo, X., Effect of manufacturing defects on optical performance of discontinuous freeform lenses. Opt. Express 2009, 17 (7), 5457-5465.
- 33. Yu, Z.; Chen, L.; Wu, W.; Ge, H.; Chou, S. Y., Fabrication of nanoscale gratings with reduced line edge roughness using nanoimprint lithography. Journal of Vacuum Science & Technology B: Microelectronics and Nanometer Structures Processing, Measurement, and Phenomena 2003, 21 (5), 2089-2092.
- 34. Zhou, P.; Burge, J., Coupling of surface roughness to the performance of computer-generated holograms. Appl. Opt. 2007, 46 (26), 6572-6576.
- 35. Zhang, Y.; Guerra-Nuñez, C.; Utke, I.; Michler, J.; Rossell, M. D.; Erni, R., Understanding and Controlling Nucleation and Growth of TiO2 Deposited on Multiwalled Carbon Nanotubes by Atomic Layer Deposition. The Journal of Physical Chemistry C 2015, 119 (6), 3379-3387.

- 36. Lalanne, P.; Astilean, S.; Chavel, P.; Cambril, E.; Launois, H., Blazed binary subwavelength gratings with efficiencies larger than those of conventional échelette gratings. Opt. Lett. 1998, 23 (14), 1081-1083.
- 37. Arbabi, A.; Arbabi, E.; Mansouree, M.; Han, S.; Kamali, S. M.; Horie, Y.; Faraon, A., Increasing efficiency of high numerical aperture metasurfaces using the grating averaging technique. Scientific Reports 2020, 10 (1), 7124.